Effects of large disorder on the Hofstadter butterfly

Chenggang Zhou,[1,*] Mona Berciu,[2] and R. N. Bhatt[1]
[1]*Department of Electrical Engineering, Princeton University, Princeton, New Jersey 08544, USA*
[2]*Department of Physics and Astronomy, University of British Columbia, Vancouver, Canada, BC V6T 1Z1*
(Received 24 December 2003; revised manuscript received 6 July 2004; published 15 March 2005)

Motivated by the recent experiments on periodically modulated, two-dimensional electron systems placed in large transversal magnetic fields [S. Melinte *et al.*, Phys. Rev. Lett. **92**, 036802 (2004)], we investigate the interplay between the effects of disorder and periodic potentials in the integer quantum Hall regime. In particular, we study the case where disorder is larger than the periodic modulation, but both are small enough that Landau level mixing is negligible. We carry extensive numerical calculations to understand the relevant physics in the lowest Landau level, such as the spectrum and nature (localized or extended) of the wave functions. Based on our results, we propose a qualitative explanation of the new features uncovered recently in these transport measurements.

DOI: 10.1103/PhysRevB.71.125310 PACS number(s): 73.43.Cd

I. INTRODUCTION

Two-dimensional electron systems (2DES) placed in a uniform perpendicular magnetic field exhibit a rich variety of phenomena, such as the integer[1] and fractional[2] quantum Hall effects,[3] and, with the addition of a periodic modulation, the Hofstadter butterfly.[4] In the latter case, the theoretical prediction of this remarkable fractal electronic structure was made in the absence of disorder. To interpret experiments, however, one must account for the effects of disorder present in any real sample.

In this paper, we investigate numerically the behavior of a 2DES subject to a perpendicular magnetic field, a periodic potential and a disorder potential, under conditions relevant for a recent experimental setup.[5] The magnetic fields are on the order of 10 T; as a result, the cyclotron energy $\hbar\omega_c = eB/mc \approx 200$ K is the largest energy scale in the problem (the effective electron mass in GaAs is $0.067m_e$). The Zeeman energy for such fields is roughly 3 K, but electron interaction effects lead to a considerable enhancement of the spin splitting between the (spin polarized) Landau levels, which has been measured to be 20 K.[6] The periodic modulation, imposed through a patterned gate, corresponds to a triangular lattice with a lattice constant of about 39 nm. The amplitude of the periodic potential's largest Fourier components is estimated to be of the order of 1 K.[7] By contrast, the scattering rate from the zero field mobility is estimated to be $\hbar/\tau \sim 8$ K,[7] showing that disorder is *large* compared to the *small* periodic modulation, although both are small enough that one can neglect Landau level (LL) mixing and study their combined effects on the electronic structure of the lowest Landau level (LLL).

Previously, the effects of *small* disorder on a Hofstadter butterfly have been perturbatively investigated using the self-consistent Born approximation (SCBA),[8,9] and the combined effect of white-noise disorder and periodic modulation on Hall resistance was studied following the scaling theory of IQHE.[10,11] If the disorder is small compared to the periodic potential amplitude, the subbands of the Hofstadter structure are "smeared" on a scale $\hbar/\tau$. The larger gaps of the butterfly remain open at the positions predicted in the absence of disorder, while the smaller gaps are closed. Such results suggest that if disorder becomes the larger term, the periodic modulation should have little or no effect on the behavior of the system. This perception may explain why, as far as we know, this case has not been theoretically investigated previously.[11]

Our study reveals a different scenario. We show that even if the periodic modulation is *small* compared to disorder, its effects on transport may be considerable if the characteristic length scale of the disorder potential is much larger than the lattice constant of the periodic potential, which is the case for high-quality, large mobility samples such as those used in Ref. 5. Our work is different in several ways. First, as already stated, we investigate the new regime of a large, long-wavelength disorder and small, short-wavelength periodic modulation, realized in recent experiments. Second, we account *exactly* for the effects of both disorder and periodic potential on the LLL, our only approximation being to neglect LL mixing (however, the techniques we develop can easily be extended to include it). This is very different from previous work based on the SCBA, which is a perturbational technique only applicable for small disorder. Third, the techniques we employ allow us to study individual disorder realizations; this is important since the signatures seen experimentally in transport are sample dependent.[5] This is also to be contrasted with SCBA, which provides only disorder-averaged quantities. As a result, it is important that we use "realistic" disorder profiles. We investigate two simplified models of disorder, one which is a sum of random Coulomb potentials and one which is a sum of random Gaussians. Both show the same qualitative behavior, leading us to conclude that the results we uncover are generic for all long-range disorder models.

The two-lead geometry we consider is sketched in Fig. 1: the finite 2DES is assumed to have periodic boundary conditions in the y-direction, and is connected to metallic leads at the $x=-L_x/2$ and $x=+L_x/2$ edges. In particular, in this paper we study the effects of the periodic potential on the extended states carrying longitudinal currents between the two leads, and identify a number of interesting properties, in qualitative agreement with simple arguments provided by a semiclassical picture and with the experimental results.

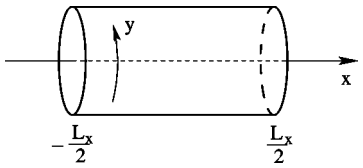

FIG. 1. The two-lead geometry considered: the finite-size 2DES has periodic boundary conditions in the y-direction, and is attached to metallic leads at the $x=\pm L_x/2$ ends.

Transport properties, such as the longitudinal conductivity, are discussed elsewhere.[12]

The paper is organized as follows: in Sec. II we briefly review the computation of the Hofstadter structure for a small-amplitude periodic potential. In Sec. III we describe the type of disorder potentials considered. Our results are presented in Sec. IV and Sec. V contains discussions and a summary of our conclusions. The numerical methods used to analyze the spectrum and the nature of the electronic states, with both semiclassical and fully quantum-mechanical formalisms, are summarized in the Appendix.

II. PERIODIC POTENTIAL

To define our notation, we review the free electron (charge $-e$) moving in the 2D xy-plane in an area of size $L_x \times L_y$, in a transversal magnetic field $\mathbf{B}=B\mathbf{e}_z$,

$$\mathcal{H} = \frac{1}{2m}\left(\mathbf{p} + \frac{e}{c}\mathbf{A}\right)^2 - \frac{1}{2}g\mu_B\vec{\sigma}\cdot\mathbf{B}.$$

For Landau gauge $\mathbf{A}=(0,Bx,0)$, the eigenstates of the Schrödinger equation $\mathcal{H}|n,k_y,\sigma\rangle = E_{n,\sigma}|n,k_y,\sigma\rangle$ are

$$\langle \mathbf{r}|n,k_y,\sigma\rangle = \frac{e^{-ik_y y}}{\sqrt{L_y}} e^{-\frac{1}{2}[(x/l)-lk_y]^2} \frac{H_n\left(\frac{x}{l}-lk_y\right)}{\sqrt{2^n n!\sqrt{\pi}l}}\chi_\sigma, \qquad (1)$$

$$E_{n,\sigma} = \hbar\omega_c\left(n+\tfrac{1}{2}\right) - \tfrac{1}{2}g\mu_B B\sigma. \qquad (2)$$

Here $l=\sqrt{\hbar c/eB}$ is the magnetic length, $\omega_c=eB/mc$ is the cyclotron frequency, $H_n(x)$ are the Hermite polynomials, and χ_σ are the eigenspinors of σ_z, $\sigma_z\chi_\sigma=\sigma\chi_\sigma$.

Cyclic boundary conditions along the y-axis imply $k_y=2\pi j/L_y$, where $j\in Z$. The wave functions are centered at $x_j=l^2k_y=l^2 2\pi j/L_y$ [see Eq. (1)] and must satisfy $-L_x/2<x_j\leqslant L_x/2$. It follows that the degeneracy of each Landau level is $N=L_xL_yB/\phi_0$, with $\phi_0=hc/e$.

Consider now the addition of a periodic potential, with a lattice defined by two noncollinear vectors $\mathbf{a}_1$ and $\mathbf{a}_2$, such that $V(\mathbf{r})=V(\mathbf{r}+n\mathbf{a}_1+m\mathbf{a}_2)$ for any $n, m\in Z$. The periodic potential $V(\mathbf{r})=\Sigma_{\mathbf{g}}V_{\mathbf{g}}e^{i\mathbf{r}\cdot\mathbf{g}}$ has nonvanishing Fourier components only at the reciprocal lattice vectors $\mathbf{g}=h\mathbf{g}_1+k\mathbf{g}_2$, where $\mathbf{g}_i\cdot\mathbf{a}_j=2\pi\delta_{ij}$ and h, k are integers. Since $V(\mathbf{r})$ is real, it follows that $V_{\mathbf{g}}=V^*_{-\mathbf{g}}$.

In the absence of LL mixing, the Hofstadter spectrum for both square,[4]

$$V_s(x,y) = 2A\left(\cos\frac{2\pi}{a}x + \cos\frac{2\pi}{a}y\right), \qquad (3)$$

and triangular,[13]

$$V_t(x,y) = -2A\left(\cos\frac{4\pi}{\sqrt{3}a}x + \cos\frac{2\pi}{\sqrt{3}a}(x-y\sqrt{3}) + \cos\frac{2\pi}{\sqrt{3}a}(x+y\sqrt{3})\right) \qquad (4)$$

periodic potentials, with nonzero Fourier components only for *the shortest reciprocal lattice vectors*, have been studied extensively in the literature.[4,9,13,14] The parameter defining the spectrum is the ratio between the flux $\phi=\mathbf{B}\cdot(\mathbf{a}_1\times\mathbf{a}_2)$ of the magnetic field through a unit cell and the elementary flux ϕ_0. For $\phi/\phi_0=q/p$, where p and q are mutually prime integers, the original Landau level is split into q subbands.

We would like to emphasize a qualitative difference between the two types of potentials: the square potential in Eq. (3) is particle-hole symmetric, since $V_s(x,y)=-V_s[x+(a/2),y+(a/2)]$. As a result, the sign of its amplitude is irrelevant. On the other hand, the triangular potential does not have this symmetry. With the sign chosen in Eq. (4) and $A>0$, V_t has deep local minima at the sites of the triangular lattice, whereas the maxima are relatively flat and located on a (displaced) honeycomb lattice. Thus, the sign of V_t is highly relevant. This choice of periodic potentials may seem restrictive because only the shortest $\mathbf{g}$ vectors are kept. In fact, the methods we employ can be used for potentials with more nonvanishing Fourier components, but their inclusion leads to no new physics.

III. DISORDER POTENTIAL

Real samples always have disorder. The current consensus is that high-quality GaAs/AlGaAs samples exhibit a slowly varying, smooth disorder potential. In a semiclassical picture, the allowed electron trajectories in the presence of such disorder follow its equipotential lines.[3,15] Closed trajectories imply localized electron states, while extended trajectories connecting opposite edges of the sample are essential for current transport through the sample (for more details, see the first section of the Appendix).

In typical experimental setups,[5] dopant Si impurities with a concentration of $\sim 10^{13}$ cm^{-2} are introduced in a thin layer of 6 nm in thickness, located 20 nm above the GaAs/AlGaAs interface. Typically, up to 10% of the Si atoms are ionized. A small fraction of the ionized electrons migrate to the GaAs/AlGaAs interface where they form the 2D electron gas. The electrostatic potential created by the ionized impurities left behind is the major source of disorder in the 2DES layer. On the length scale we are interested in, there are 10^4 to 10^5 such ionized Si impurities per μm^2. The resulting disorder potential must be viewed as a collective effect of the density fluctuation of the ionized impurities[16] rather than a simple summation of the Coulomb potential of

a few impurities. The electrostatic potential from Si impurities is compensated and partially screened by other mobile negative charges in the system such as, for example, the surface screening effect by mirror charges considered by Nixon and Davies.[16] An exact treatment of this problem is difficult, since one should consider the spatial correlation of the ionized impurities.[17,18] One model used to describe such disorder consists of randomly placed Gaussian scatterers.[19] This model captures the main feature of a smooth disorder potential and supports classical trajectories on equipotential contours, but it has no natural energy/length scales associated with it. As a result, here we choose to also investigate a different model of the disorder, which incorporates the smooth character of the Coulomb potential in real space.

We generate a realization of the disorder potential in the following way: positive and negative charges, corresponding to a total concentration of 10^3 $\mu\mathrm{m}^{-3}$ are randomly distributed within a volume $[-L_x/2, L_x/2]\times[-L_y/2, L_y/2]\times[20\ \mathrm{nm}+d, 26\ \mathrm{nm}+d]$ above the electron gas which is located in the $z=0$ plane. Here, we choose $d=4$ nm as an extra spacer since the electronic wave functions are centered about 3–5 nm below the GaAs/AlGaAs interface. Since we are not simulating single impurities but density fluctuations, these charges are not required to be elementary charges. Instead, we use a uniform distribution in the range $[-e, e]$ for convenience (a Gaussian distribution would also be a valid choice), and sum up all Coulomb potentials from these charges, using the static dielectric constant in GaAs $\epsilon = 12.91$.[20] The resulting disorder potential has energy and length scales characteristic of the real samples. Typical contours for such potentials are shown in Sec. IV.

In an infinite system, in the quantum Hall regime, the existence of quantum Hall steps implies the existence of critical energies at which the localization length diverges.[21] This is the quantum analog of the two-dimensional percolation problem in a smooth random landscape, for which there exists a single critical energy.[15] In the case of potentials with electron-hole symmetry $\langle V(\mathbf{r})\rangle = 0$, the critical energy lies in the middle of the band ($E_c = 0$), leading to percolating path at half-filling. For a finite mesoscopic sample, however, not only does the percolating path (critical energy) E_c deviate from this value, but in samples without a periodic boundary condition one need not have a percolating path traversing the system in the desired direction. This arises from the fluctuations near the edge of a mesoscopic system with free boundary conditions.

We circumvent such a possibility by adding an extra smooth potential $V'(x,y)$ to the impurity-induced disorder potential $V_i(x,y)$, such that the total potential $V = V_i + V'$ is zero on the opposite edges $x = \pm L_x/2$ of the sample where the metallic leads are attached. The supplementary contribution $V'(x,y)$ can be thought of as simulating the effect of the leads on the disorder potential, since the metallic leads hold the potential on each edge constant by accumulating extra charges near the interface. Therefore, physically we expect that the extra potential V' decays exponentially over the screening length λ inside the sample. This implies

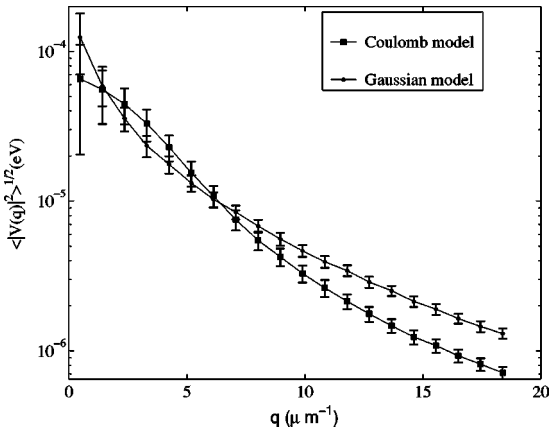

FIG. 2. Averaged Fourier amplitudes of two types of disorder potential as a function of wave vector $q=|\mathbf{q}|$. For both Coulomb and Gaussian model, $V(q)^2$ is averaged over 116 disorder realizations. The relation between $V(q)$ and $V(\mathbf{r})$ and relevant parameters are discussed in the text. The standard deviation, $(L_xL_y)^{-1}\langle\int d\mathbf{r}\, V^2(\mathbf{r})\rangle$ for the Coulomb model is 3.2×10^{-7} eV^2, and 2.1×10^{-7} eV^2 for the Gaussian model.

$$V'(x,y) = -\frac{V_i(-L_x/2,y)+V_i(L_x/2,y)}{2}\frac{\cosh(x/\lambda)}{\cosh(L_x/2\lambda)} + \frac{V_i(-L_x/2,y)-V_i(L_x/2,y)}{2}\frac{\sinh(x/\lambda)}{\sinh(L_x/2\lambda)},$$

where λ is taken to be 100 nm in our calculation.

In Fig. 2, we plot the average of Fourier transform of the magnitude of the random potential $\sqrt{\langle|V(q)|^2\rangle}$ versus $q=|\mathbf{q}|$ for the Coulomb model and the Gaussian model. The Gaussian model is generated by adding 100 randomly placed Gaussian scatterers on an area of 3 μm$\times$3 μm, each contributing $A_d e^{-r^2/d^2}$, where A_d is uniformly distributed between $[-2,2]$ meV, and d is uniformly distributed in [0, 0.2] μm. $V(\mathbf{q})$ is related to $V(\mathbf{r})$ by $V(\mathbf{r})=\Sigma_{\mathbf{q}}V(\mathbf{q})e^{i\mathbf{q}\cdot r}$, where the summation is over all the wave vectors involved in the fast Fourier transformation. $V(q)$ of both models are decreasing functions of q, with exponential decay at large q. At small q, the two models behave differently. Despite the difference, both models lead to the same qualitative results, although, as expected, minor quantitative differences are present. This shows that the physics we uncover is independent of the particular type of slowly varying disorder potential considered, and thus should be relevant for real samples.

IV. RESULTS

In this section we present typical numerical results we obtain using the methods summarized in the Appendix. We have analyzed over 20 different disorder realizations for samples of different sizes; all exhibit the same qualitative physics. The lattice constant is always $a=39$ nm if the periodic potential is present.[5]

First, we consider a sample with $L_x=3.11$ μm and $L_y=76a=2.964$ μm for $\phi/\phi_0=3/2(B=4.71\ \mathrm{T})$. The magnetic length is $l=12.03$ nm and each Landau level contains

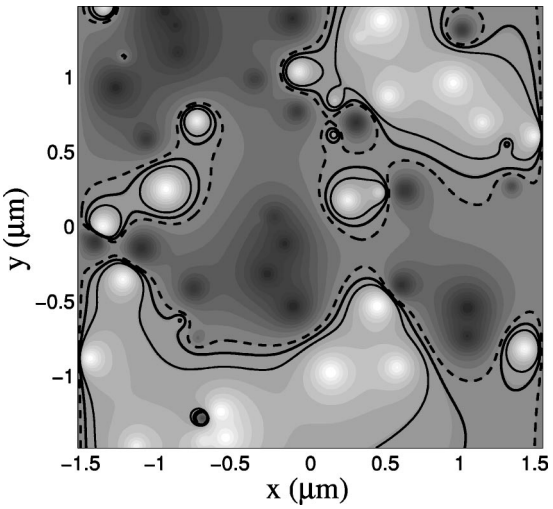

FIG. 3. Profile of the disorder potential obtained from our Coulomb model on a 3.11 μm$\times$2.96 μm sample with the $V'(\mathbf{r})$ correction at the $x=\pm L_x/2$ edges. The disorder potential varies between −3 meV and 3 meV, on a spatial length-scale much larger than $l=12.03$ nm. The critical region containing extended states is in the vicinity of $E=0.06$ meV. The contours are shown for $E=0.0575$ meV (dashed), 0.17 meV (thick solid), and 0.31 meV (thin solid). These energy values correspond to classical filling factors $\nu=0.45$, 0.56, 0.66.

$N=10\,108$ states. The disorder potential obtained with our scheme described in Sec. III, including the correction $V'(\mathbf{r})$, is shown in Fig. 3. An extended equipotential line appears, as expected, at $\nu\approx 0.5$.

In Figs. 4 and 5 we plot, for the LLL, the filling factor $\nu(E)$ and the corresponding total density of states (DOS) $\rho(E)$ as a function of E (for computational details see the Appendix). These quantities are obtained in the semiclassical limit (dashed line) and with the full, quantum-mechanical treatment (solid line). Results are shown for four different cases: (a) only disorder potential and (b), (c), (d) disorder

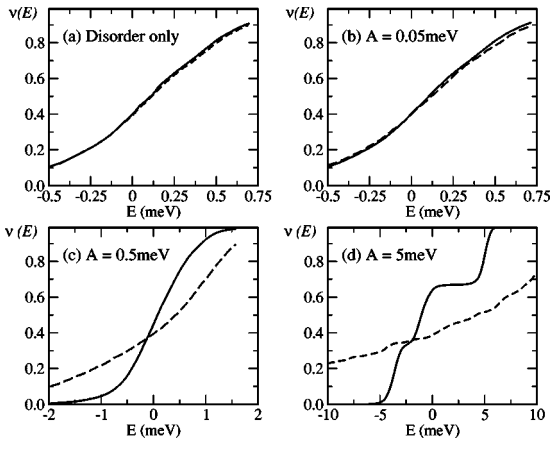

FIG. 4. Semiclassical (dashed line) and quantum (solid line) filling factors for the disorder potential shown in Fig. 3, but different amplitudes of the triangular periodic potential (a) $A=0$, (b) $A=0.05$ meV, (c) $A=0.5$ meV, and (d) $A=5$ meV. As expected, agreement exists only in the limit $A\to 0$.

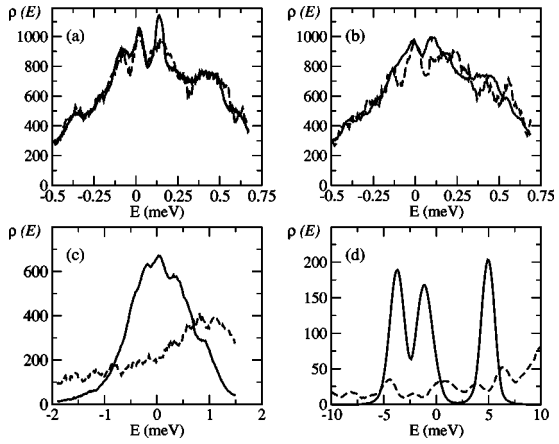

FIG. 5. Semiclassical (dashed line) and quantum (full line) density of states calculated from corresponding filling factors in Fig. 4. We show only the center of the disorder-broadened lowest Landau level, where the density of states is large.

plus a triangular periodic potential with amplitudes $A=0.05$, 0.5, and 5 meV, respectively. We show only a relatively small energy interval where the DOS is significant, and ignore the asymptotic regions with long tails of localized states.

While the agreement between the semiclassical and quantum-mechanical treatment is excellent in the limit $A\to 0$, the two methods give more and more different results as the periodic potential amplitude is increased. This is a consequence of the fact that the magnetic length l is comparable to the lattice constant a, leading to a failure of the semiclassical treatment when this new short length scale is introduced. In particular, in the case with the largest periodic potential [panel (d) of Figs. 4 and 5] we can clearly see the appearance of the three subbands expected for the Hofstadter butterfly at $\phi/\phi_0=3/2$, although the disorder leads to broadened and smooth peaks, and partially fills-in the gap between the lower two subbands. This picture [panel (d)] is quite similar to the density of states calculated in Ref. 8 using the self-consistent Born approximation. This is expected since the SCBA approach is valid in the limit of strong periodic potential with weak disorder. However, the SCBA approach is not appropriate in the limit of moderate or strong disorder. For disorder varying on a much longer length scale than the periodic potential, one still expects that *locally*, on areas where disorder is relatively flat, the system exhibits the Hofstadter-type spectrum. However, these "local" spectra are shifted with respect to one another by the different local disorder values. If disorder variations are small, then the total spectrum shows somewhat shifted subbands with partially filled-in gaps, but overall the Hofstadter structure is still recognizable. On the other hand, for moderate and large disorder, the detailed structure of the local density of states from various flat regions are hidden in the total density of states. All one sees are some broadened, weak peaks and gaps superimposed on a broad, continuous density of states.

We now analyze the nature of the electronic states for these configurations. We start with the case which has only disorder. In Fig. 6 we plot the matrix elements of the Green's function between LL states on the opposite sides of the sample, $|G^R(k_{\min},k_{\max};E)|^2$ as a function of the energy E.

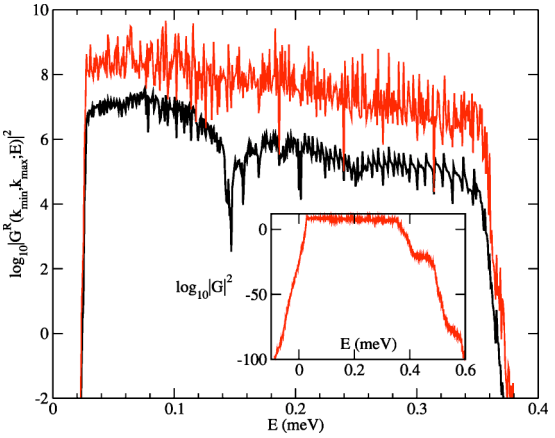

FIG. 6. Semilog plot of the amplitude of Green's function matrix element between the two edge states near $x=\pm L_x/2$, as a function of energy, for $\delta=10^{-7}$ eV (black line) and $\delta=10^{-8}$ eV (grey line). δ is the small imaginary part in the Green's function, see the Appendix. Only the disorder potential of Fig. 3 is applied in this calculation. Inset, the same quantity for $\delta=10^{-8}$ eV, over a larger energy range.

The results shown are for a small imaginary energy $\delta=10^{-7}$ and 10^{-8} eV in the denominator of the Green's function, Eq. (A4) (for computation details see the Appendix). As discussed in the Appendix, extended states are indicated by large values of this matrix element, as well as a strong (roughly $1/\delta^2$) dependence on the value of the small parameter δ. Figure 6 reveals that as δ is reduced, resonant behavior appears in a narrow energy interval $E=0.02$–0.36 meV, where results for the two δ values indeed differ by roughly 2 orders of magnitude, with $\delta=10^{-8}$ eV showing sharper resonance peaks. The value of the Green's function decreases exponentially fast on both sides of the critical region (see inset of Fig. 6), indicating strongly localized states. We conclude that the disorder potential has a critical energy regime of $\sim$0.3 meV width, covering less than 5% (in energy) and 20% (in number of states) of the disorder-broadened band with total width $\sim$6 meV. The position of the critical energy interval is in agreement with the semiclassical results which suggest an extended state in the vicinity of $E=0.06$ meV. By comparison with Fig. 4, we can also see that this critical regime indeed corresponds to a roughly half-filled band.

The effect of adding a triangular periodic potential is shown in Fig. 7, where we plot the same quantity shown in Fig. 6 for a fixed $\delta=10^{-7}$ eV and different amplitudes $A=0$, 0.05, 0.5, and 5 meV, respectively. These results correspond to a different Coulomb disorder potential (not shown), as can be seen from the different location of its extended states. The narrow critical region of extended states widens as the amplitude of the periodic potential increases. For the largest A value, the three Hofstadter subbands of extended states, expected for $\phi/\phi_0=3/2$, are clearly visible. The three subbands can already be resolved for the moderate amplitude $A=0.5$ meV, although they have significant overlap.

Qualitatively similar behavior is obtained if we use the Gaussian scatterers model for disorder. A typical realization of this disorder is shown in Fig. 8. Results for the Green's function's values with such disorder are shown in Fig. 9, for

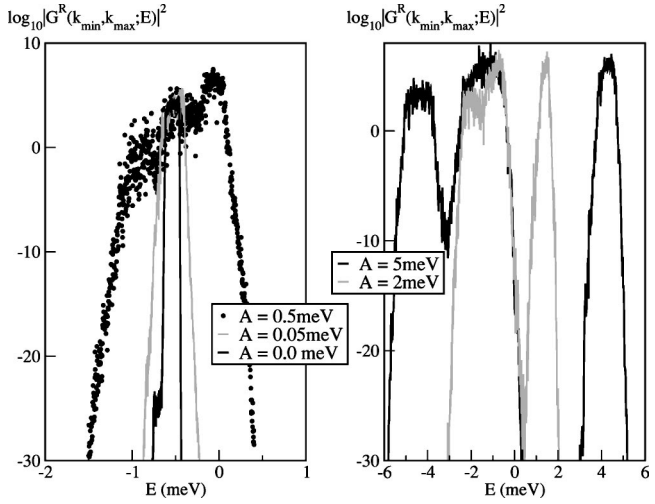

FIG. 7. The effect of a triangular periodic potential on the critical energy regime. The disorder potential used here (not shown) supports a narrow interval of extended states centered at about −0.6 meV. As the amplitude A of the periodic potential increases, the range of extended states increases dramatically. The left panel shows results for disorder-only and two relatively weak periodic potentials, while the right panel shows two larger periodic potentials where the three-subband structure expected for $\phi/\phi_0=3/2$ is clearly seen.

cases with pure disorder, and also cases with either a triangular or a square periodic potential. The magnetic field has been doubled, such that $\phi/\phi_0=3$. Similar to results in Fig. 7, the periodic potential leads to a widening of the critical regime. For large periodic potentials, the expected Hofstadter three-subband structure emerges again. We conclude that Coulomb and Gaussian disorder models show qualitatively similar behavior.

We now analyze the projected local density of states $\rho_P(\vec{r},E)$ (for details, see the Appendix) to understand the

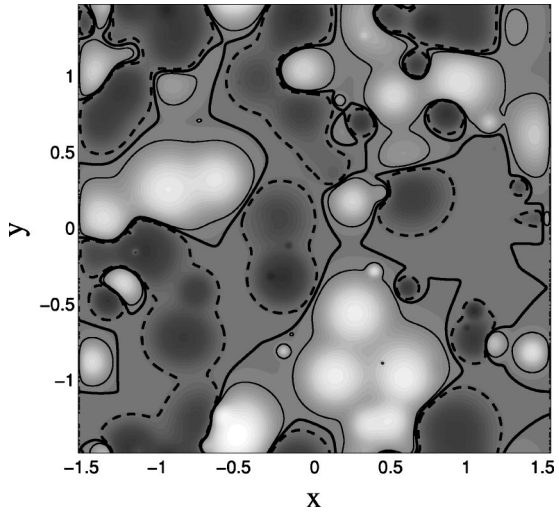

FIG. 8. A disorder potential of Gaussian type on a roughly 3 μm$\times$3 μm square. The three lines are equipotential contours close to the critical regime, with energies of −0.1 meV (dashed), 0 meV (thick solid), and 0.1 meV (thin solid). Cyclic boundary condition are applied in the y direction.

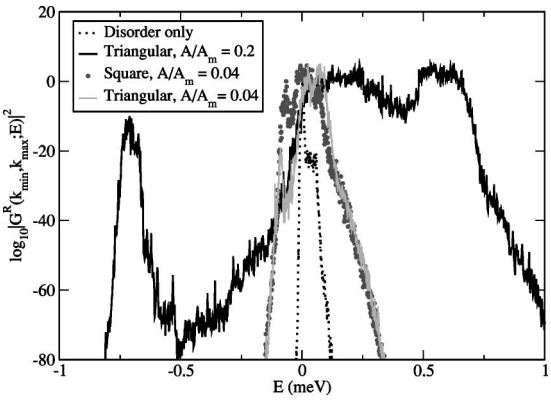

FIG. 9. Green's functions for a sample with Gaussian disorder and various periodic potentials. The calculation included 20216 states with $\phi/\phi_0=3$. Similar to results shown in Fig. 9, we see that the periodic potentials widen the critical region.

reason for this substantial widening of the critical region by even small periodic potentials. We consider a smaller sample, of about 1.6 μm$\times$1.6 μm. We compute the projected density of states at positions $\vec{r}$ on a 60×60 square grid, for 500 equally spaced energy values and for $\delta=10^{-8}$ eV. This δ value is comparable or smaller than the level spacing, so we expect to see sharp resonances from the contribution of individual eigenfunctions as we scan the energy spectrum. Each computation generates a large amount of data (roughly 24M), for the 500 plots of $\rho_P(\vec{r},E)$. We select a couple of representative cases and some statistical data to interpret the overall results.

Figures 10 and 11 show some of our typical results. The two figures are calculated for the same Coulomb-disorder potential, for values of $E=-0.504$ meV (at the bottom of the band) and $E=-0.124$ meV (close to, but below the band center), respectively. Each figure contains four panels. Panel (a) shows the profile of the disorder potential as well as an equipotential line (solid black) corresponding to the value E considered; the other three panels show the projected density of states $\rho_P(\vec{r},E)$ for (b) pure disorder; (c) disorder plus triangular periodic potential with $A=0.1$ meV; (d) disorder plus square periodic potential with $A=0.1$ meV. In Fig. 10, the equipotential line (which traces the semiclassical trajectory of electrons with the same energy E) surrounds local minima of the disorder potential, suggesting localized electron states at such low energies. Indeed, this is what panels (b), (c), and (d) show. The projected density of states $\rho_P(\vec{r},E)$ is large (bright color) at the positions where electrons of energy E are found with large probabilities. For pure disorder, we observe only closed trajectories (localized states), whose shape is in excellent agreement with the semiclassical trajectory, as expected. If a moderate periodic potential is added, the wave-functions spread over a larger area, and nearby contours sometimes merge together. Instead of sharp lines, as seen in panel (b), the contours now show clear evidence of interference effects of the wave functions on the periodic potential decorating the electron reservoirs. Some periodic modulations can also be observed in the background of panels (c) and (d), especially for the square potential. These are *not* the direct oscillations of the periodic potentials, since the grid we use to compute these figures has a linear size equal to 7/10 of the period $a=39$ nm of the periodic potential. Capturing detailed behavior inside each unit cell would require a much smaller grid, which is not only time consuming, but also violates the requirement that the grid size be of order l or larger.

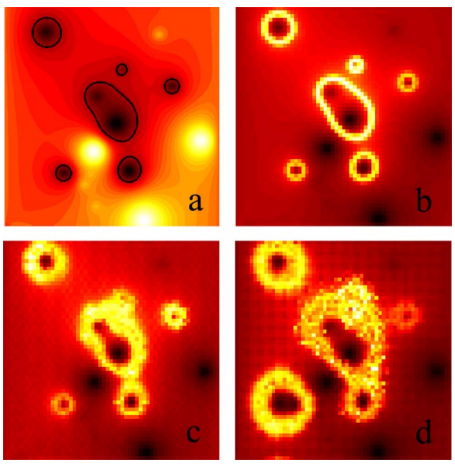

FIG. 10. (Color online) Projected local density of states $\rho_P(\mathbf{r};E)$ for $E=-0.504$ meV. Panel (a) shows the profile of the disorder potential, and the equipotential contour (black line) corresponding to $E=-0.504$ eV. The other three panels show $\rho_P(\mathbf{r};E)$ for (b) disorder only; (c) disorder plus triangular periodic potential with $A=0.1$ meV; (d) disorder plus square periodic potential with $A=0.1$ meV. The width and length of the sample are both 1.6 μm, and $\phi/\phi_0=3/2$. Increased brightness corresponds to larger values.

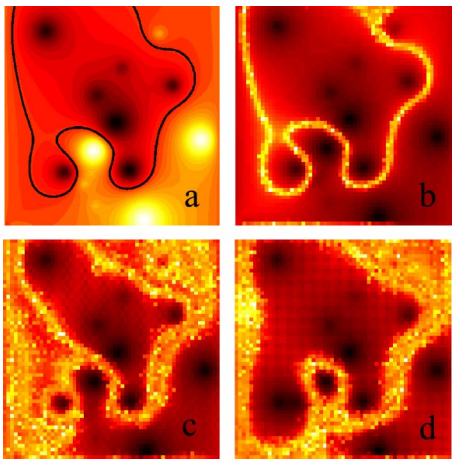

FIG. 11. (Color online) The same as in Fig. 10, but for an energy $E=-0.124$ meV close to the band center.

Figure 11 for an energy close to the band center shows the same characteristics. For pure disorder, the electrons at this energy trace a sharp contour very similar to the corresponding equipotential line shown in panel (a). Electrons are still not delocalized, since this contour does not connect either pair of opposite edges. However, addition of the periodic potential now leads to an extended state for both types of periodic potentials [(c) and (d)], demonstrating the widening of the critical region with the addition of a periodic potential.

Physically, one can understand this spread of the wave function in the presence of the periodic potential using the

semiclassical picture.[5] If only a smooth disorder potential is present, the equipotential at any energy E must be a smooth, continuous line. However, if a periodic potential with minima $-V_m$ and maxima V_M is superimposed over disorder, the new equipotential line now breaks into a series of small "bubbles" surrounding the disorder-only contour. These appear throughout the area defined by the equipotentials $E-V_M$ and $E+V_m$ of the disorder potential, since the addition of the periodic potential leads new regions in this area to have a total energy E. Quantum mechanically, we expect some tunneling inside this wider area and this is indeed what we observe in Figs. 10 and 11. This mechanism suggests *enhanced delocalization* on both sides of the critical region as localized wave functions spread out over larger areas, as well as a widening of the critical region itself, in agreement with our numerical results.

This spreading of the wave functions in the presence of the periodic potential can also be characterized by counting, at a given energy E, the number of grid points $\mathbf{r}$ which have a value $\rho_P(\mathbf{r};E)>\rho_c$, where ρ_c is some threshold value. For sufficiently large ρ_c, this procedure counts grid points where electrons with energy E are found with large probabilities, thus, in effect it characterizes the "spatial extent" of the wave functions. The results of such counting are shown in Fig. 12 for 500 energy values corresponding to the disorder potential analyzed in Figs. 10 and 11. There are a total of $60\times 60=3600$ grid points on the sample. For the case of pure disorder (black line) we see that the largest values are found at energies just below 0, where the extended states (the critical region) are found for this particular realization of disorder. Because it is a smooth, sharp line, even the most extended trajectory has significant probabilities at only about 10% of the grid sites. For both higher and lower energies, this number decreases very fast, indicating wave functions localized more and more about maxima or minima in the disorder potential, as expected. Addition of a small periodic potential increases this number substantially, clearly showing the supplementary spreading of the wave functions in the presence of the periodic potential.

Figure 12 shows this effect for three types of periodic potential: triangular lattices with $A>0$ and $A<0$ (upper panel), and square lattice in the lower panel. All three cases show significant enhancement, as compared to the pure disorder case. In addition, we see that while the square potential gives a fairly symmetrical enhancement, the triangular potential does not, with curves for $\pm A$ not overlapping. This is a consequence of the asymmetric shape of the periodic potential, which has different values for its minima and maxima $|V_m|\neq|V_M|$, as well as different arrangements for the points where minima/maxima appear (triangular lattice vs honeycomb lattice). Figure 12 clearly shows that $A>0$ favors increased delocalization below the critical energy regime, while $A<0$ favors increased delocalization above it.

The reason for this different response to the two signs of the triangular potential can be nicely explained within the semiclassical framework. In Fig. 13 we show the equipotential lines corresponding to filling factors $\nu=0.3$ (well below critical region) and $\nu=0.7$ (well above the critical region) for a realization of Coulomb disorder (not shown) plus a triangular potential with $A>0$. Areas with energy below the equi-

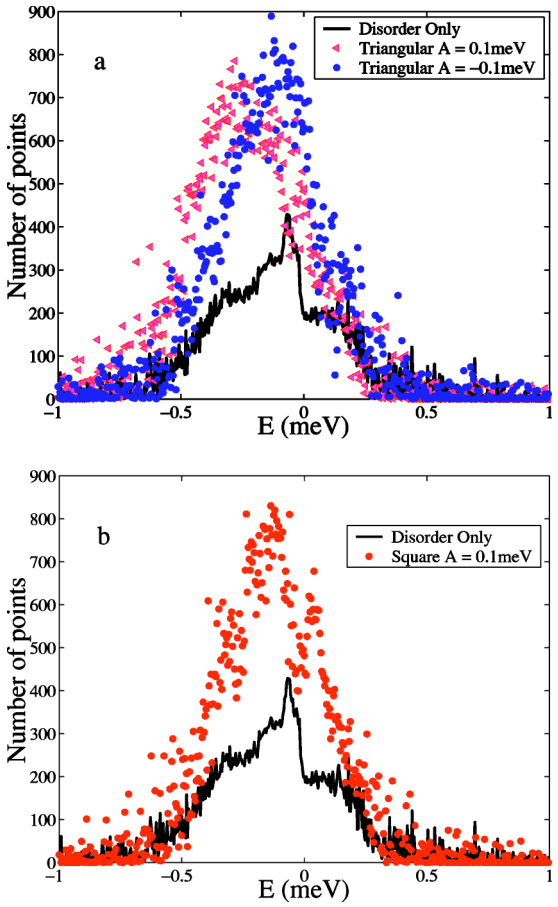

FIG. 12. (Color online) Number of grid points for which $\rho_P(\mathbf{r};E)>100$ as a function of E. This quantity characterizes the "spatial extent" of the wave function. The upper panel compares results for disorder only ($A=0$) and disorder plus triangular potentials with $A\pm 0.01$ meV. The difference observed for the two signs is a consequence of particle-hole asymmetry of the triangular potential. The lower panel shows results for disorder only and disorder plus a square potential.

potential value are shaded. We see that instead of the continuous, smooth trajectory expected for disorder-only cases, there are also periodic "bubbles" regions connecting the areas between such contours. Since the choice $A>0$ leads to deep minima at $-V_m=-6A$ with triangular arrangement and relatively flat maxima at $+V_M=3A$ with honeycomb arrangement [see Eq. (4)], it follows that the triangular (honeycomb) "bubbles" region appear roughly in the area bounded by the equipotentials E and $E+V_m$ (respectively, $E-V_M$ and E) of the pure disorder potential. At low filling factors, the pure disorder E equipotential is a collection of closed contours surrounding local minima [see panel (d) of Fig. 10 for an illustration]. It follows that for the choice $V_m>V_M$, the more extended region with triangular "bubbles" will be found outside these "islands" and will lead to a spread of the wave function over considerably larger areas, as indeed seen in the upper panel of Fig. 13. On the other hand, at large filling factors the triangular "bubbles" between E and $E+V_m$ are inside the disorder E contour, and do not help to enhance percolation. The smaller areas (since $V_M<V_m$) of honeycomb "bubbles" do this, but much less effectively.

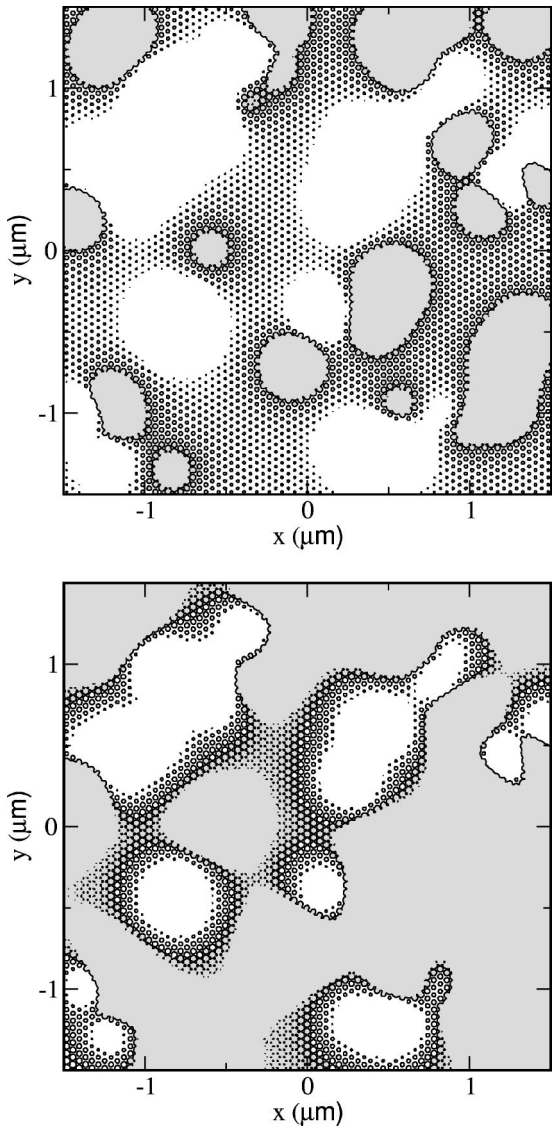

FIG. 13. Equipotential contours at filling factor $\nu=0.3$ (upper panel) and $\nu=0.7$ (lower panel) for a 3 μm$\times$3 μm sample with disorder plus a small triangular periodic potential with $A>0$. The shaded regions correspond to energies below the respective equipotential. In the semiclassical approximation, the shaded areas are filled with electrons, with the maximum density of $1/2\pi l^2$, whereas the white areas are completely devoid of electrons. Quantum-mechanically, one expects interference in the regions with small periodic "bubbles," induced by the periodic potential (see Figs. 10 and 11).

In the quantum-mechanical case one expects interference (due to tunneling) within the "bubbles" regions, and therefore a wave function which is extended over their entire area, as indeed we observe to be the case in Figs. 10 and 11. In other words, one expects that a triangular potential with $A>0$ will lead to considerable increase of the localization length, and, respectively, widening of the critical energy region, at filling factors below one-half, whereas $A<0$ will favor delocalization at filling factors above one-half, as seen in Fig. 12. This asymmetry is therefore clearly a consequence of the asymmetry of the triangular potential, and is absent for a particle-hole symmetric square potential. This has clear effects on the transport properties of the system.

V. SUMMARY AND CONCLUSIONS

We have investigated the effects of moderate-to-large, long-range disorder on the Hofstadter butterfly expected for 2DES in a perpendicular magnetic field and a pure periodic modulation. The parameters of our study are chosen so as to be suitable for the interpretation of a recent experiment on a modulated 2DES.[5] The experiment shows that (i) the longitudinal resistance R_{xx} is still peaked approximately at half-filling; (ii) there are many reproducible oscillations in R_{xx}, indicating nontrivial electronic structures in the patterned sample; (iii) the distribution of these oscillatory features is asymmetric, with most of them appearing on the high magnetic fields (i.e., low filling factors $\nu<0.5$) side of the peak of R_{xx}; and (iv) the temperature dependence of R_{xx} indicates that the asymmetric off-peak resistance is thermally activated, whereas the central R_{xx} peak (close to half-filling) has metallic behavior.

These observations cannot be explained on the basis of the Hofstadter structure.[5] This is not surprising, since one expects that large disorder will modify the butterfly considerably. Effects of small disorder on the Hofstadter butterfly had been investigated previously using SCBA,[8] but this basically perturbational approach is not appropriate for the case of moderate-to-large disorder. Instead, we identify and use a number of techniques which give the exact solution (if electron-electron interactions, as well as inelastic scattering are neglected) while avoiding brute force numerical diagonalizations.

Our results demonstrate that while the Hofstadter butterfly is destroyed by large disorder, the effects of the periodic potential are nontrivial for states near the critical regime. First, they lead to a significant increase in localization lengths of the localized states at mesoscopic (μm) length scale and induce an effective widening of the critical regime. This is achieved through a spreading of the electron wave function on the flat regions of the slowly varying disorder potential, where their behavior is dominated by the periodic modulation.

This regime shows an interesting transition between the pure disorder and the pure periodic potential cases. In the case of pure disorder, the semiclassical approach predicts that at finite filling factors, areas of the sample where $V_d(\mathbf{r})<E_F$ are filled with electrons with the maximum density of $1/(2\pi l^2)$ whereas areas where $V_d(\mathbf{r})>E_F$ have no electrons. Moreover, the boundary between such regions is very sharp. On the other hand, for a pure periodic modulation all wave functions have translational invariance with the proper symmetry, and therefore electron densities are uniform over the entire sample (up to small periodic modulations inside each unit cell). When both types of potential are present, with disorder being dominant, our results show *three* types of areas. There are regions which are fully occupied and regions which are completely devoid of electrons, as in the case of pure disorder. However, the periodic potential leads to a widening of the boundary between the two, where

the wave functions interact with several oscillations of the periodic modulation and therefore have some partial local filling. Such regions have a Hofstadter-type local electronic structure. If the partial filling factor in such a region is inside the gap of the local Hofstadter butterfly, one expects no transport through this local area, leading to a decrease in the total longitudinal conductivity. By contrast, if the local filling factor in such a region is inside a subband of a local Hofstadter structure, the resulting wave function will increase the percolation, leading to an enhancement of the transport through the sample. Transport in this regime should show strong thermal activated behavior, in contrast to metallic transport in the critical regime where extended wave functions connect opposite edges of the sample.

As a result, one expects a series of local minima and maxima in the longitudinal resistivity on either side of the central peak induced by the extended states (critical regime). Furthermore, for an asymmetric triangular potential, this response should be strongly asymmetric, with the effect most visible on one side of the central peak. (One must keep in mind that since tunneling leads to exponential dependencies, even small differences in the extent of the wave functions can have rather large effects on ρ_{xx}.) Such an asymmetry should also be present in longitudinal conductance at finite but low temperature, e.g., in the hopping regime which is sensitively dependent on the nature of the localized wave functions, as is indeed seen experimentally.[5]

To summarize, our qualitative explanation for the various experimental features are as follows:

(i) The R_{xx} peak is roughly at the center of the band because the weak periodic potential cannot establish a Hofstadter-type structure over the whole band. Instead, low and high ν states remain strongly localized.

(ii) New extended states induced by the periodic potential are responsible for the reproducible peaks and valleys appearing in R_{xx}.

(iii) The periodic potential also leads to the expansion of localized wave functions, which contribute to the thermally activated conduction at lower filling factors. The detailed structure of the wave functions gives rise to the oscillations of the off-peak R_{xx}, similar to conductance fluctuations.[22]

(iv) The asymmetry in R_{xx} is a manifestation of the asymmetry of the triangular potential, which has a stronger effect at low filling factors than at high filling factors for $A>0$. We predict that this asymmetry should be absent for a symmetric square periodic potential.

The weak point in our calculation is that we are unable to accurately model the potential in the real samples, because various screening effects have not been properly taken into account. Also, we have no quantitative information about the magnitude of the periodic potential in the 2DES layer, because of the additional strain[23] contribution induced by the periodic decoration. As a result, we only claim qualitative agreement with the experiment, although our investigations show the same type of behavior for various types of disorder potentials and various (small-to-moderate) strengths of the periodic potential. The most direct check of this work would be an experimental demonstration that thermally activated conduction appears symmetrically on both sides of the R_{xx} peak for a periodic potential with square symmetry.

Limited computer resources restrict our calculations to samples no larger than $3\ \mu\mathrm{m}\times 3\ \mu\mathrm{m}$, while the sample used in the experiment has a size of $20\ \mu\mathrm{m}\times 20\ \mu\mathrm{m}$. From a theoretical point of view, it is interesting to ask what is the thermodynamic limit. For pure disorder, it is believed that in this limit the typical size of wave function diverges at a single critical energy. As we cannot pursue size-dependent analysis, we do not know whether the small periodic potential will lead to a finite size critical regime, although this seems likely. Our results for these mesoscopic samples are consistent with previous work on the different effects of attractive and repulsive scattering centers.[29] We expect that in the thermodynamic limit, the asymmetric effect of the triangular potential will lead to shifts in R_{xx} similar to those found in Ref. 29, because the triangular potential is predominantly attractive or repulsive depending on the sign of its amplitude. On the other hand, the order of potential minima (maxima), either a local or a global order, which is absent in the calculation of Ref. 29, will enhance the non-Born scattering, believed to cause the shift in ρ_{xx} minima in Ref. 29. From an experimental point of view, the interesting question is whether the Hofstadter structure can be observed at all. Our studies suggest that this may be possible for small mesoscopic samples, where the slowly varying disorder has less effect. Alternatively, one must find a way to boost the strength of the periodic modulations inside the 2DES.

ACKNOWLEDGMENTS

The authors thank S. Melinte, M. Shayegan, P. Chaikin, and M. Wu for valuable discussions. The authors also thank Professor Li Kai's group in the Computer Science Department of Princeton University for sharing their computer cluster with us. This research was supported by NSF Grant No. DMR-213706 (C.Z. and R.N.B.) and by NSERC (M.B.).

APPENDIX: NUMERICAL METHODS

In this appendix we summarize the numerical methods we used, including derivations of some relevant formulas.

Semiclassical treatment

The semiclassical approach is valid[15] for the integer quantum Hall effect in the presence of a slowly varying, smooth disorder potential and large magnetic fields (such as we consider), so that the magnetic length l is much smaller than the length scale of variation of the smooth disorder potential, $|\nabla V(\mathbf{r})| \ll \hbar\omega_c/l$. Then, semiclassically the electron moves along the equipotential contours of the disorder potential $V(\mathbf{r})$, in the direction parallel to $\nabla V(\mathbf{r})\times\mathbf{B}$. Since the kinetic energy is quenched in the lowest Landau level, the total energy of the electron simply equals the value of the disorder potential on the equipotential line on which its trajectory is located. As a result, the density of states in the semiclassical approach is directly given by the probability distribution for the disorder potential, which can be calculated by randomly sampling the potential energy and plotting a histogram of the obtained values.[15,24]

In Sec. IV we compared the results obtained within this semiclassical approach with fully quantum mechanical results. As expected, the agreement is good when only the slowly varying disorder is present. However, if the periodic modulation is also included, the lattice constant a provides a new length-scale which is comparable to the magnetic length l, and the semiclassical picture breaks down. Quantum mechanical calculations are absolutely necessary to quantitatively treat this case.

Quantum mechanical treatment

As shown in Sec. II, the degeneracy of each LL is $N = L_x L_y B/\phi_0 = L_x L_y/(2\pi l^2)$. Since the disorder varies very slowly, we need to consider systems with $L_x, L_y \gg l$ to properly account for its effects. As a result, the number of states in a LL can be as large as 10^4 in our calculations. Storage of the Hamiltonian as a dense matrix requires considerable amount of computer memory and its direct diagonalization is prohibitively time consuming. Sparse matrix diagonalization techniques could be employed, but they are less efficient when all eigenvectors are needed, and may have stability issues.

Here we describe the numerical methods we used to compute densities of states and infer the nature (localized or extended) as well as the spatial distribution of the wave functions, while avoiding direct diagonalization.

Matrix elements

Since interlevel mixing is ignored, the Hilbert subspaces corresponding to different spin-polarized Landau levels do not hybridize. Each Hilbert subspace (n,σ) has a basis described by Eq. (1), containing N orthonormal vectors indexed by different k_y values.

In order to compute matrix elements of the total Hamiltonian in such a basis, we use the following identity derived in Ref. 9 (Notice their different sign convention for k_y. If $\sigma \neq \sigma'$, the overlap is zero):

$$\langle n', k_y' | e^{i\mathbf{q}\cdot\mathbf{r}} | n, k_y \rangle = \delta_{k_y', k_y - q_y} \mathcal{L}_{n',n}(\mathbf{q}) e^{(il^2/2) q_x (k_y' + k_y)}, \quad \text{(A1)}$$

where

$$\mathcal{L}_{n',n}(\mathbf{q}) = \left(\frac{m!}{M!}\right)^{\frac{1}{2}} i^{|n'-n|} \left[\frac{q_x + iq_y}{\sqrt{q_x^2 + q_y^2}}\right]^{n-n'} \times e^{-\frac{1}{2}Q} Q^{\frac{1}{2}|n'-n|} L_m^{(|n'-n|)}(Q),$$

with $Q = \frac{1}{2} l^2 (q_x^2 + q_y^2)$, m and M are the minimum and the maximum of n' and n, respectively, and $L_m^{(|n'-n|)}(Q)$ the associated Laguerre polynomial. When band-mixing is neglected $n = n'$ and $\mathcal{L}_{n,n}(\mathbf{q}) = e^{-\frac{1}{2}Q} L_n(Q)$. For the first Landau level, $L_0(x) = 1$.

Equation (A1) gives us the matrix elements for the square [Eq. (3)] or triangular [Eq. (4)] periodic potentials. In either case, there are Fourier components corresponding to $q_y = \pm 2\pi/a$ and $q_y = 0$. Since only basis vectors for which the difference $k_y - k_y' = q_y$ give nonvanishing matrix elements, we must choose the length L_y of the sample to be a multiple integer of a, the lattice constant.

The matrix elements of the disorder potential are computed in a similar way. We use a grid of dimension $N_x \times N_y$ to cover the sample and generate the values of the disorder potential on this grid. Then, fast Fourier transform (FFT)[25] is used to find the long wavelength components of the disorder potential corresponding to the allowed values $q_{x,y} = 0, \pm(2\pi/L_{x,y}), \ldots, \pm(N_{x,y}/2)(2\pi/L_{x,y})$ (proper care is taken to define Fourier components so that $V_{\mathbf{q}} = V_{-\mathbf{q}}^*$). The matrix elements of this discretized disorder potential are then computed using Eq. (A1). In principle, finer grids (increased values for N_x and N_y) will improve accuracy. However, they also result in longer computation times, since they add extra matrix elements in the sparse matrix, corresponding to large wave vectors. We have verified that a grid size of dimension $N_x = N_y = 72$ is already large enough to accurately capture the landscape of a $3\ \mu\text{m} \times 3\ \mu\text{m}$ sample and the computed quantities have already converged, with larger grids leading to hardly noticeable changes. This procedure is also justified on a physical basis. First, the neglected large wave-vector components describe very short-range spatial features, which are not accurately captured by our disorder models to begin with, and which are not believed to influence the basic physics. Second, this procedure insures that the actual disorder potential we use is periodic in the y-direction, since each Fourier component retained has this property. This is consistent with our use of a basis of wave functions which are periodic along y.

The matrix elements of the Hamiltonian within a given Landau level (n,σ) are then $\langle n, k_y, \sigma | \mathcal{H} | n, k_y', \sigma \rangle = E_{n,\sigma} + \langle n, k_y | \mathcal{V} | n, k_y' \rangle$, where $E_{n,\sigma}$ are given by Eq. (2) and the matrix elements of both the periodic and the disorder part of the potential $\mathcal{V}$ are computed as already discussed. This produces a sparse matrix, which is stored efficiently in a column compressed format.

Densities of states and filling factors

A quantity that can be computed without direct diagonalization is the filling factor. In the absence of LL mixing, we define the filling factor for the (n,σ) LL as

$$\nu_{n,\sigma}(E_F) = \frac{1}{N} \sum_{\alpha} \Theta(E_F - E_{n,\alpha,\sigma}), \quad \text{(A2)}$$

where $\Theta(x)$ is the Heaviside function and N is the degeneracy of the LL. The filling factor is the fraction of occupied states at $T = 0$, for a given Fermi energy E_F. It corresponds to the average filling factor measured in experiment and is proportional to the integrated total (as opposed to local) density of states.

The filling factor is straightforward to compute if the eigenenergies $E_{n,\alpha,\sigma}$ are known. However, we want to avoid the time-consuming task of numerical brute force diagonalization. The strategy we follow is a generalization to Hermitian matrices of the method used in Ref. 26. We restate the problem in the following way: assume we have a Hermitian matrix of size $N \times N$, given by the matrix elements of $M = \mathcal{H} - E_F \mathbf{1}$ in the basis $|n, k_y, \sigma\rangle$ ($\mathbf{1}$ is the unit matrix).

Then, $\nu_{n,\sigma}(E_F)$ is proportional to the number of negative eigenvalues of the matrix M. We now generate the quadratic form $\mathcal{M}=\Sigma_{i,j=1}^{N}\zeta_i\zeta_j^* M_{ij}$, and transform it into its standard form $\mathcal{M}=\Sigma_{i1}^{N} d_i|\chi_i|^2$ using the Jacobian method described below. Here, d_i's are all real numbers, and the χ_i's are linear combinations of the ζ_i's. This is a similarity transformation which retains the signature of the matrix. As a result, even though the numbers d_i are not eigenvalues of M, the number of negative eigenvalues equals the number of negative d_i values. It follows that $\nu_{n,\sigma}(E_F)$ is obtained by simply counting the number of negative d_i values for the given E_F.

The Jacobian method is iterative in nature. First, all terms containing ζ_1 and ζ_1^* are collected and the needed complementary terms are added to form the first total square $d_1|\chi_1|^2$. The procedure is then repeated for all ζ_2 and ζ_2^* terms (producing d_2), etc., until all N values d_i are found. Computationally, this can be done by scanning the lower or upper triangle of the Hermitian matrix M only once. The total number of operations is proportional to the number of nonzero elements of the matrix, meaning that for a dense matrix it scales with N^2 (sparse matrices require much fewer operations). As a result, this procedure is much faster than brute force diagonalization which scales with N^3 (for us, $N\sim 10^4$). The filling factor $\nu_{n,\sigma}(E)$ is a sum of steplike functions, with steps located at the eigenvalues. By scanning E and identifying the position of these steps we can also find the true eigenvalues $E_{n,\alpha,\sigma}$, with the desired accuracy. Finally, the total density of states is given by $\rho_{n\sigma}(E)=\mathrm{d}\nu_{n,\sigma}(E)/\mathrm{d}E$.

Green's functions: extended vs localized states

The advanced/retarded Green's functions are the solutions of the operator equation

$$(\hbar\omega-\mathcal{H}\pm i\delta)\hat{G}^{R,A}(\omega)=\mathbf{1}, \tag{A3}$$

where $\delta\to 0^+$. (In practice we use a set of small positive numbers, as discussed later). If the exact eigenstates and eigenvalues of the total Hamiltonian $\mathcal{H}$ are known, $\mathcal{H}|n,\alpha,\sigma\rangle=E_{n,\alpha,\sigma}|n,\alpha,\sigma\rangle$ (no LL mixing), it follows:

$$\hat{G}^{R,A}(\omega)=\sum_{n,\alpha,\sigma}\frac{|n,\alpha,\sigma\rangle\langle n,\alpha,\sigma|}{\hbar\omega-E_{n,\alpha,\sigma}\pm i\delta}=\sum_{n,\sigma}\hat{G}^{R,A}_{n,\sigma}(\omega). \tag{A4}$$

The exact eigenstates can be expanded in terms of the basis states $|n,k_y,\sigma\rangle$ as

$$|n,\alpha,\sigma\rangle=\sum_{k_y}c_{n,\alpha}(k_y)|n,k_y,\sigma\rangle. \tag{A5}$$

Since the states $|n,k_y,\sigma\rangle$ are localized near $x=k_y l^2$ [see Eq. (1)], the coefficients $c_{n,\alpha}(k_y)$ describe the probability amplitude for an electron in the state $|n,\alpha,\sigma\rangle$ to be located within a distance l from $x=k_y l^2$. Knowledge of these coefficients allows us to infer whether such states are extended or localized in the x-direction, i.e., whether they can carry currents between the leads.

However, we wish to avoid direct diagonalization. We can still infer whether the Hamiltonian has extended or localized wave functions near a given energy $\hbar\omega$ in the following way. We introduce the matrix elements,

$$G^{R,A}_{n,\sigma}(k_y,k_y';\omega)=\langle n,k_y,\sigma|\hat{G}^{R,A}(\omega)|n,k_y',\sigma\rangle=\sum_{\alpha}\frac{c_{n,\alpha}(k_y)c^*_{n,\alpha}(k_y')}{\hbar\omega-E_{n,\alpha,\sigma}\pm i\delta}. \tag{A6}$$

Equation (A3) can be rewritten in the basis $|n,k_y,\sigma\rangle$ as

$$\sum_{k_y''}[(\hbar\omega\pm i\delta)\delta_{k_y,k_y''}-\langle n,k_y,\sigma|\mathcal{H}|n,k_y'',\sigma\rangle]G^{R,A}_{n,\sigma}(k_y'',k_y';\omega)=\delta_{k_y,k_y'}. \tag{A7}$$

We use the popular numerical library SuperLU,[27] based on LU decomposition and Gaussian reduction algorithm for sparse matrices, to solve these linear equations. Consider now the matrix element $G^{R,A}_{n,\sigma}(k_{\min},k_{\max};\omega)$ corresponding to the smallest $k_y=k_{\min}$ and the largest $k_y=k_{\max}$ values. If all wave functions with energies close to $\hbar\omega$ are localized in the x-direction, it follows that $|G^{R,A}_{n,\sigma}(k_{\min},k_{\max};\omega)|$ is a very small number, of the order $e^{-L_x/\xi(\omega)}$, where $\xi(\omega)$ is the localization length at the given energy. On the other hand, we expect to see a sharp peak in the value of $|G^{R,A}_{n,\sigma}(k_{\min},k_{\max};\omega)|$ if $\hbar\omega$ is in the vicinity of an extended state eigenvalue, since [see Eqs. (A5) and (A6)] both $c_{n,\alpha}(k_{\min})$ and $c_{n,\alpha}(k_{\max})$ are nonvanishing for an extended wave function with significant weight near both the $-L_x/2$ and the $L_x/2$ edges. Moreover, the height of this peak scales like $1/\delta$, so by varying δ we can easily locate the energies of the extended states.

Green's functions: local densities of states

We can also use Green's functions techniques to image the local density of states at a given energy E. By definition (and neglecting LL mixing), the local density of states in the level (n,σ) is

$$\rho_{n,\sigma}(\mathbf{r};E)=\sum_{\alpha}|\langle\mathbf{r}|n,\alpha,\sigma\rangle|^2\delta(E-E_{n,\alpha,\sigma})=\frac{1}{\pi}\mathrm{Im}\langle\mathbf{r}|\hat{G}^{A}_{n,\sigma}(E)|\mathbf{r}\rangle, \tag{A8}$$

where the second equality follows from Eq. (A4). This function traces the contours of probability $|\langle\mathbf{r}|n,\alpha,\sigma\rangle|^2$ for electrons with the given energy E. Its direct computation, however, is very time-consuming.

For the rest of this section, the discussion is restricted to the LLL with $n=0$; the value of σ is irrelevant. We know that in the LLL, electronic wave functions cannot be localized in any direction over a length-scale shorter than the magnetic length l. As a result, it suffices to compute a projected local density of states on a grid with $l\times l$ (or larger) spacings. The projection is made on maximally localized wave function, defined as follows. Let $\mathbf{r}_0=(x_0,y_0)$ be a point on the grid. We associate it with a vector

$$|x_0,y_0\rangle=\sum_{k_y}|k_y\rangle\langle k_y|x_0,y_0\rangle, \tag{A9}$$

where we use the simplified notation $|k_y\rangle\equiv|n=0,k_y,\sigma\rangle$ for the basis states of the LLL [see Eq. (1)] and we take

$$\langle k_y|x_0,y_0\rangle = \sqrt{\frac{2l\pi^{\frac{1}{2}}}{L_y}} e^{-(x_0^2/2l^2)-(k_y^2l^2/2)+k_y(x_0+iy_0)}. \quad \text{(A10)}$$

It is then straightforward to show that

$$\langle \mathbf{r}|x_0,y_0\rangle = \frac{1}{\sqrt{2\pi l}} e^{-[(x-x_0)^2/4l^2]-[(y-y_0)^2/4l^2]} e^{-(i/2l^2)(x+x_0)(y-y_0)}. \quad \text{(A11)}$$

In other words, $|x_0,y_0\rangle$ is an eigenstate of the lowest Landau level strongly peaked at $\mathbf{r}=\mathbf{r}_0$. (The phase factor is due to the proper magnetic translation.) We then define the projected density of states [compare with Eq. (A8)],

$$\rho_P(x_0,y_0;E) = \frac{1}{\pi}\mathrm{Im}\langle x_0,y_0|\hat{G}^A(E)|x_0,y_0\rangle, \quad \text{(A12)}$$

and use it to study the spatial distribution of the electron wave functions at different energies. Strictly speaking, the local density of states defined in Eq. (A8) cannot be projected exactly on the LLL, because the LLL does not support a δ-function ($\langle \mathbf{r}|n,k_y,\sigma\rangle \neq 0, \forall n$). However, the coherent states $|x_0,y_0\rangle$ we select are the maximally spatially localized wave functions in the LLL, and have the added advantage that they can be easily stored as sparse vectors, because of their Gaussian profiles [see Eq. (A10)]. Moreover, in the limit $l\to 0 (B\to\infty)$ where $|\langle \mathbf{r}|x_0,y_0\rangle| \to \delta(x-x_0)\delta(y-y_0)$, the projected density of states $\rho_P(x_0,y_0;E)\to\rho_{0,\sigma}(\mathbf{r};E)$. Therefore, for the large B values that we consider here, ρ_P should provide a faithful copy of the local density of states.

We compute the projected local density of states following the method of Ref. 28. Let $\mathbf{u}_0$ be the vector with elements $\langle k_y|x_0,y_0\rangle$ obtained from the representation of $|x_0,y_0\rangle$ in the $|k_y\rangle$ basis [see Eq. (A9)], and let H be the matrix of the Hamiltonian $\mathcal{H}$ in the $|k_y\rangle$ basis. We generate the series of orthonormal vectors $\mathbf{u}_0$, $\mathbf{u}_1$, … using

$$\mathbf{v}_1 = H\mathbf{u}_0, \quad a_0\mathbf{u}_0^\dagger\mathbf{v}_1, \quad \mathbf{u}_1 = \frac{\mathbf{v}_1 - a_0\mathbf{u}_1}{\sqrt{\mathbf{v}_1^\dagger\mathbf{v}_1 - a_0^2}}$$

and for $n\geqslant 2$, $\mathbf{v_n}=H\mathbf{u}_{n-1}$, $a_{n-1}=\mathbf{u}_{n-1}^\dagger\mathbf{v_n}$, $b_{n-2}=\mathbf{u}_{n-2}^\dagger\mathbf{v_n}$, and

$$\mathbf{u}_n = \frac{\mathbf{v}_n - a_{n-1}\mathbf{u}_{n-1} - b_{n-2}\mathbf{u}_{n-2}}{\sqrt{\mathbf{v}_n^\dagger\mathbf{v}_n - a_{n-1}^2 - b_{n-2}^2}}.$$

The numbers a_n and b_n can be shown to be real. We do not have a "terminator"[28] to end this recursive series. Instead, our procedure ends when the orthonormal set of vectors $\mathbf{u}_0$, $\mathbf{u}_1$, … exhausts a subspace of the LLL containing all states coupled through the disorder and/or periodic potential to the state $|x_0,y_0\rangle$, i.e., all states that contribute to the projected DOS at this point. In the presence of disorder, this usually includes the entire LLL.

Then, the projected density of states is given by Eq. (A12), where the matrix element of the Green's function is the continued fraction

$$\langle x_0,y_0|G^A(E)|x_0,y_0\rangle = \{E - i\delta - a_0 - b_0^2[E - i\delta - a_1 - b_1^2(\cdots)^{-1}]^{-1}\}^{-1}. \quad \text{(A13)}$$

Because the Hamiltonian is a sparse matrix, the generation of these orthonormal sets and computation of $\rho_p(E)$ for all the grid points is a relatively fast procedure. Moreover, this computation is ideally suited for parallelization, with different grid points assigned to different CPUs.

*Present address: Oak Ridge National Laboratory, P.O. Box 2008 MS 6164, Oak Ridge, Tennessee 37831-6164, USA.

[1] K. v. Klitzing, G. Dorda, and M. Pepper, Phys. Rev. Lett. **45**, 494 (1980).
[2] D. C. Tsui, H. L. Störmer, and A. C. Gossard, Phys. Rev. Lett. **48**, 1559 (1982).
[3] For a review, see *The Quantum Hall Effect*, edited by R. E. Prange and S. M. Girvin, Graduate Texts in Contemporary Physics (Springer-Verlag, New York, 1987).
[4] D. R. Hofstadter, Phys. Rev. B **14**, 2239 (1976).
[5] S. Melinte, M. Berciu, C. Zhou, E. Tutuc, S. J. Papadakis, C. Harisson, E. P. De Poortere, M. Wu, P. M. Chaikin, M. Shayegan, R. N. Bhatt, and R. A. Register, Phys. Rev. Lett. **92**, 036802 (2004).
[6] S. Melinte, E. Grivei, V. Bayot, and M. Shayegan, Phys. Rev. Lett. **82**, 2764 (1999), and references therein.
[7] P. Chaikin (private communication).
[8] U. Wulf and A. H. MacDonald, Phys. Rev. B **47**, 6566 (1993).
[9] D. Pfannkuche and R. R. Gerhardts, Phys. Rev. B **46**, 12 606 (1992).
[10] B. Huckstein and R. N. Bhatt, Surf. Sci. **305**, 438 (1994).
[11] There is a considerable amount of work on the effects of disorder on the Hofstadter butterfly, for tight-binding models. Such models correspond to having the periodic modulation as the dominant energy scale, and investigate the interplay between disorder potential and the cyclotron energy scales. This is very different from the regime of interest to us, where the cyclotron energy is the dominant scale while disorder competes with the periodic modulation.
[12] C. Zhou and M. Berciu, Phys. Rev. B **70**, 165318 (2004).
[13] F. H. Claro and G. H. Wannier, Phys. Rev. B **19**, 6068 (1979).
[14] D. Springsguth, R. Ketzmerick, and T. Geisel, Phys. Rev. B **56**, 2036 (1997).
[15] S. A. Trugman, Phys. Rev. B **27**, 7539 (1983).
[16] J. A. Nixon and J. H. Davies, Phys. Rev. B **41**, 7929 (1990).
[17] M. Stopa, Phys. Rev. B **53**, 9595 (1996); Physica B **227**, 61 (1996).
[18] S. Das Sarma and S. Kodiyalam, Semicond. Sci. Technol. **13**, A59 (1998).
[19] T. Ando, J. Phys. Soc. Jpn. **53**, 3101 (1984).
[20] R. Williams, *Modern GaAs Processing Methods* (Artech House, Boston, London, 1990).
[21] B. I. Halperin, Phys. Rev. B **25**, 2185 (1982).

[22] J. A. Simmons, H. P. Wei, L. W. Engel, D. C. Tsui, and M. Shayegan, Phys. Rev. Lett. **63**, 1731 (1989).
[23] J. H. Davies and I. A. Larkin, Phys. Rev. B **49**, 4800 (1994).
[24] Allowed trajectories are such that the total flux through the area enclosed by the trajectory is an integer number of elementary fluxes ϕ_0. This can be understood in the spirit of the Bohr–Sommerfeld quantization rule, since it ensures constructive interference of the wave function around the contour. Except for the most localized states, found at the bottom and the top of the band, all other localized states are such that they enclose large numbers of magnetic fluxes. Imposing the exact quantization condition (which is numerically time consuming) leads to a negligible change in the value of the allowed equipotential value with respect to a randomly chosen value. Since such small changes do not influence the shape of the density of states, we ignore imposing this quantization condition in obtaining the semiclassical densities of states.
[25] We used the package FFTW2.1.3 available on-line at http://www.fftw.org
[26] C. Zhou and R. N. Bhatt, Phys. Rev. B **68**, 045101 (2003).
[27] M. Baertschy, T. N. Rescigno, W. A. Isaacs, X. Li, and C. W. McCurdy, Phys. Rev. A **63**, 022712 (2001). Details regarding the software also available at http://www.nersc.gov/xiaoye/SuperLU
[28] R. Haydock, Phys. Rev. B **61**, 7953 (2000).
[29] R. J. Haug, R. R. Gerhardts, K. v. Klitzing, and K. Ploog, Phys. Rev. Lett. **59**, 1349 (1987).